Stability Analysis and Interaction-Rule-Based Optimization of Multisource and Multiload DC Microgrid

Ling Yang, *Member, IEEE*, Zehang Huang, *Student Member, IEEE*, Jinghua Chen, Jianqiang Luo, *Member, IEEE*, Yu Wang, *Member, IEEE*, Marta Molinas, *Fellow, IEEE*, and Olav Bjarte Fosso, *Senior Member, IEEE*

***Abstract*—Coupling interaction within multisource and multiload (MSML) challenges the stable operation of dc microgrids. To disclose the essential mechanism, a detailed small-signal model of the MSML dc microgrid is established first. Then, the relations between coupling parameters and stability margin are investigated using modal analysis and participation factor. Two important corollaries are discovered: 1) in a three-source system, when the sources distribute in the two long and one short of the transmission lines, the system can achieve the largest stability margin; and 2) the increase of power sources will induce an impedance augmentation effect and improve the stability margin. Thus, an interaction-rule-based optimization method is proposed to adjust the controller parameters, which can not only raise damping and improve stability margin but also provide inertia for the system. Substantial theoretical analyses and hardware-in-the-loop experiments further verify these findings and the effectiveness of the proposed method.**

***Index Terms*—DC microgrid, interaction-rule-based optimization, multisource and multiload (MSML), stability analysis.**

I. Introduction

THE increasing penetration of renewable energy makes dc microgrids widely concerned [1]. DC microgrids need neither reactive compensation nor frequency and phase control, which can reduce power loss and ensure high efficiency with simple control [2], [3], [4]. In addition, energy storage resources can be easily integrated into the dc distribution system, making distributed generations (DGs) more popular. Most loads are connected to the dc microgrids by power electronic converters and are usually represented as constant power loads (CPLs). However, CPL exhibits a negative impedance that makes dc bus voltage sensitive. This may lead to instability and reduce power quality in some circumstances. Therefore, with the integration of DGs and CPLs, multisource and multiload (MSML) dc microgrid becomes a hot research topic [5], [6], [7].

The primary control of the dc–dc converter includes inner loop control (current/voltage regulation) and droop control (power sharing) [8]. In the MSML system, droop control has been widely used to avoid dependence on communication lines [9]. Power generation of DG is intermittent, which can lead to acute fluctuation in dc bus voltage and incur harmful effects on DGs and CPLs. Therefore, virtual inertial control is introduced to improve the voltage quality of the dc bus. At present, a variety of virtual inertial control methods are proposed, including variable droop coefficient, supplementary differential control, and analogized virtual synchronous machine [10]. Considering the inertial support of island model, it is necessary to establish an MSML system with droop control and virtual inertial control, which is more congruent with the practical engineering requirements.

The research focus of dc microgrid operation is stability analysis [11]. Major methods for small-disturbance stability analysis include impedance analysis [12], [13] and eigenvalue analysis [14], [15]. Impedance analysis focuses on the external characteristics of the study object. Eigenvalue analysis can characterize the key information of the dynamic stability of the system, including the distribution of oscillation and the contribution of state variables to the oscillation [16]. This information is indispensable for the optimizing overall layout and control strategy of the dc microgrids [17]. Therefore, the eigenvalue analysis is an effective method to analyze small-disturbance stability [18].

The method of eigenvalue analysis studies the system stability by analyzing the trajectory of the eigenvalues [19], [20]. Scholars have done a lot of research on the key parameters that affect the stability of dc microgrids, mainly including parameters of transmission line, the number of sources/loads, and control parameters. In [21], a reduced-order linearized system model is established, which proves that the stability margin of the

Manuscript received 29 March 2023; revised 25 July 2023; accepted 9 October 2023. Date of publication 23 October 2023; date of current version 6 December 2023. This work was supported in part by the National Natural Science Foundation of China under Grant 52107185, and in part by the Natural Science Foundation of Guangdong Province under Grants 2023A1515010061, 2021A1515012398, and 2021A1515010742. Recommended for publication by Associate Editor J. Liu. *(Corresponding author: Jianqiang Luo.)*

Ling Yang, Zehang Huang, Jinghua Chen, Jianqiang Luo, and Yu Wang are with the School of Automation, Guangdong University of Technology, Guangzhou 510006, China (e-mail: yangling_1992@163.com; huangzh4444@163.com; 43884010@qq.com; jqluo@gdut.edu.cn; yuwang@gdut.edu.cn).

Marta Molinas is with the Department of Engineering Cybernetics, Norwegian University of Science and Technology, 7491 Trondheim, Norway (e-mail: marta.molinas@ntnu.no).

Olav Bjarte Fosso is with the Department of Electric Power Engineering, Norwegian University of Science and Technology, 7491 Trondheim, Norway (e-mail: olav.fosso@ntnu.no).

Color versions of one or more figures in this article are available at https://doi.org/10.1109/TPEL.2023.3326484.

Digital Object Identifier 10.1109/TPEL.2023.3326484

system can be increased when the equivalent resistance of the transmission line increases or the equivalent inductance decreases. At the present stage, the research is still focused on the length of a single transmission line [22], [23]. However, there is no research on the influence of the mutual matching of transmission line lengths among DGs on the system stability, so it is necessary to study the line layout in the MSML system. In [24] and [25], eigenvalue analysis is used to discuss the instability risk caused by the same DGs or CPL aggregation. In the mechanism analysis, most of the existing work summarizes some rules, which draw graphical results but cannot explain the essential mechanism. For the case of DGs connecting to the power grid, the existing research is that with the increase in the number of DGs, the total output power of the DGs will also increase, which is not conducive to stability [26]. At present, the internal mechanism of the relationship between the number of DGs and the system stability is rarely studied, especially in the case of constant total power under islanded operation.

It is worth noting that the study of the influence of multicontrol parameter interaction on system stability is still limited. The existing research is mainly based on the model of multicontrol with a single source or single control with multisource. In [27], the influence of the interaction between the phase-locked loop and voltage regulator on the stability margin of high-voltage dc transmission systems is studied under weak grid. This strategy only establishes a model of the single source to study the interaction of different control parameters and does not take into account the influence of multisource; thus, it exhibits limitations. A coupled droop control strategy is proposed to study the influence of droop gain on system stability after multisource [28]. In this method, a multisource model is established, but the interaction between other control loops and droop control is ignored. In [29], considering virtual inertia control and droop control, the influence of multisource control combination on system stability is studied. However, this study did not address the impact of the interaction of two control parameters on the stability of the multisource model. As a result of the above problems, it is difficult to determine the parameter range and adjustment direction of the MSML system. Therefore, it is necessary to study the interaction between multicontrol parameters in the multisource model.

There are three methods to improve the stability of dc microgrids: adding damping loop; installing suppression device; and optimizing parameter [30], [31], [32], [33]. The additional damping loop can be effectively controlled for a specific frequency band. However, when the operating point of the system changes, the control parameters of the damping loop cannot be adjusted accordingly. The installation of the suppression device is applicable to projects that have been put into operation. It is flexible and simple, but the cost is high. Parameter optimization can quickly improve the system stability without changing the control structure and increasing cost. This method is relatively direct and effective. In [32], particle swarm optimization (PSO) is used to determine the optimal droop values of the dispatchable DGs in order to simultaneously reduce the fuel cost, increase system damping, and push the most dominant eigenvalue away from the imaginary axis to the left of the complex plane. In [33], an optimal operation of a droop-controlled stand-alone dc microgrid with combined small-signal stability and economic-environment-related objectives is proposed. However, the above literature adopts a single control factor in the process of parameter optimization. The interaction of multiple control parameters is not considered for optimization.

Based on the above analysis, the system presents the following challenges.

1) At present, the impact of transmission lines on system stability is still in qualitative or quantitative analysis of the change law of single line length. However, when there are numerous power sources, the problem of how to coordinate transmission lines to optimize system stability is rarely studied.
2) Currently, many studies focus on how the variation of overall load power affects the system stability as the number of power sources changes. Nevertheless, while the system's overall load power remains constant, the influence of the number of power sources on the system stability gets little research.
3) Most of the research on the optimization method of control parameters is based on the artificial intelligence algorithm to obtain the optimal parameters, which has certain limitations on the adaptability of working conditions. However, the optimization method based on the interaction of control parameters is rarely considered.

The main contributions of this article are as follows.

1) When three sources are used for power supply, the stability margin is greater when the source-side line is "two long and one short (TLOS)" than when it is "two short and one long (TSOL)." The reason for the difference is that the coupling degree of state variables in the dominant modes affects the change of the eigenvalues' real part.
2) When the load power of the system is constant, the system stability can be improved by increasing the number of power sources. The increase in the number of power sources will enhance the equivalent impedance of the source side, resulting in the impedance augmentation effect (IAE).
3) Considering the interaction of virtual inertia coefficient and droop coefficient on the system stability, an optimization method of control parameters based on the interaction rule is proposed to improve the system stability and make multisource provide more inertia. Compared with the results of PSO, the proposed method is more satisfactory.

The rest of this article is organized as follows. Section II establishes a full-order small-signal MSML DC microgrid model and calculates the eigenvalues. In Section III, the influence of transmission lines, multisource, and multiload on stability margin of the system is studied. Section IV examines the interaction of virtual inertia control and droop control parameters between multiple sources and proposes an interaction-rule-based optimization method. Section V builds a hardware-in-the-loop experimental platform based on the model. Finally, Section VI concludes this article.

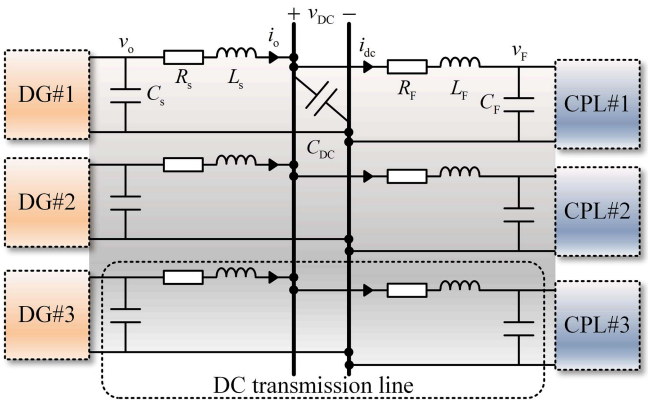

Fig. 1. Structure diagram of MSML DC microgrid.

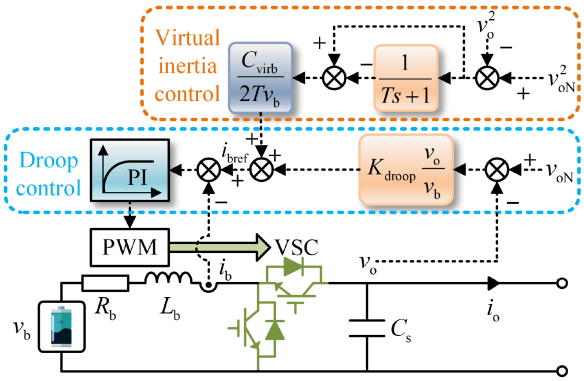

Fig. 2. Control strategy diagram of DG.

II. Small-Signal Modeling of DC Microgrid

The MSML dc microgrid composes of DGs, dc transmission lines, and CPLs, as shown in Fig. 1. Next, small-signal modeling of each part is carried out.

A. Small-Signal Modeling of DG

As shown in Fig. 2, the DG adopts droop control and virtual inertia control of a bidirectional dc–dc converter. Droop control ensures the power distribution among multiple sources. Virtual inertia control is similar to the working principle of the capacitor, aiming to improve the system inertia and regulate the dynamic behavior of dc bus voltage. d is the duty ratio of the bidirectional converter. v_b and i_b are voltage and current before the conversion of DG, respectively. i_bref is the reference value of i_b. v_o and i_o are the outlet voltage and current after conversion, respectively. v_oN is the rated value of v_o. R_b, L_b, and C_s are parasitic resistance, filter inductance, and support capacitance, respectively. S_v is the output after square deviation of v_oN and v_o passes through the first-order inertia loop. S_i is the integral process of proportional–integral (PI) current loop. T is the time constant. s is the Laplace operator. K_droop is the droop coefficient. C_virb is the virtual inertia coefficient. k_p and k_i are the proportional and integral coefficients of the PI current loop, respectively. The state-space model of DG is shown in (1), and the small-signal model of DG is shown in (2)

$$\begin{cases} L_\mathrm{b}\frac{di_\mathrm{b}}{dt} = v_\mathrm{b} - (1-d)v_\mathrm{o} - R_\mathrm{b}i_\mathrm{b} \\ \frac{dS_\mathrm{v}}{dt} = \frac{1}{T}(v_\mathrm{oN}^2 - v_\mathrm{o}^2 - S_\mathrm{v}) \\ \frac{dS_\mathrm{i}}{dt} = i_\mathrm{bref} - i_\mathrm{b} \\ S_\mathrm{v} = \frac{1}{Ts+1}\frac{v_\mathrm{oN}^2 - v_\mathrm{o}^2}{s} \\ i_\mathrm{bref} = K_\mathrm{droop}\frac{v_\mathrm{o}}{v_\mathrm{b}}(v_\mathrm{oN} - v_\mathrm{o}) + \frac{C_\mathrm{virb}}{2Tv_\mathrm{b}}(v_\mathrm{oN}^2 - v_\mathrm{o}^2 - S_\mathrm{v}) \\ d = k_\mathrm{p}(i_\mathrm{bref} - i_\mathrm{b}) + k_\mathrm{i}S_\mathrm{i} \end{cases} \tag{1}$$

$$\frac{d\boldsymbol{x}_\mathrm{b}}{dt} = \boldsymbol{A}_\mathrm{b}\boldsymbol{x}_\mathrm{b} + \boldsymbol{B}_\mathrm{b}\boldsymbol{v}_\mathrm{o} \tag{2}$$

where $\boldsymbol{x}_\mathrm{b} = [\Delta i_\mathrm{b}, \Delta S_\mathrm{v}, \Delta S_\mathrm{i}]^T$ and $\boldsymbol{v}_\mathrm{o} = [\Delta v_\mathrm{o}]^T$. The presence of "$\Delta$" indicates the state variable.

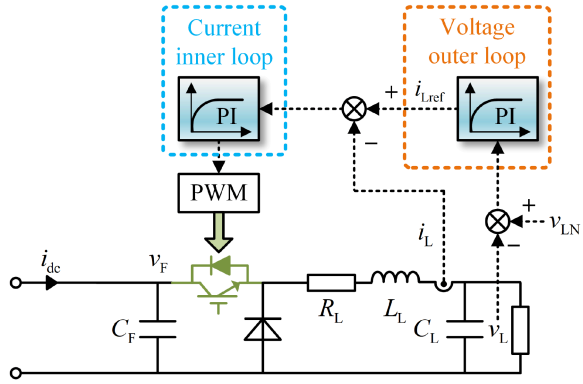

Fig. 3. Control strategy diagram of CPL.

B. Small-Signal Modeling of CPL

As shown in Fig. 3, the CPL adopts a buck circuit for voltage conversion and the double-loop control strategy of voltage–current. g is the duty ratio of the buck circuit. v_F, v_LN, and v_L are the inlet voltage before CPL conversion, rated voltage, and actual voltage of CPL, respectively. i_dc is the current before the conversion. i_L and i_Lref are the current of CPL and its reference value, respectively. R_L and C_F are the parasitic resistance and support capacitance of the load side, respectively. L_L and C_L are filter inductance and filter capacitance, respectively. S_vL is the integral process of the PI outer loop. S_iL is the integral process of the PI inner loop. k_vLp and k_vLi are the proportional and integral coefficients of the PI outer loop, respectively. k_iLp and k_iLi are the proportional and integral coefficients of the PI inner loop, respectively. P_L represents the power of CPL. The state-space model of CPL is shown in (3), and its small-signal model is shown in (4)

$$\begin{cases} L_\mathrm{L}\frac{di_\mathrm{L}}{dt} = gv_\mathrm{F} - v_\mathrm{L} - R_\mathrm{L}i_\mathrm{L} \\ C_\mathrm{L}\frac{dv_\mathrm{L}}{dt} = i_\mathrm{L} - \frac{P_\mathrm{L}}{v_\mathrm{L}} \\ \frac{dS_\mathrm{vL}}{dt} = v_\mathrm{LN} - v_\mathrm{L} \\ \frac{dS_\mathrm{iL}}{dt} = i_\mathrm{Lref} - i_\mathrm{L} \\ i_\mathrm{Lref} = k_\mathrm{vLp}(v_\mathrm{LN} - v_\mathrm{L}) + k_\mathrm{vLi}S_\mathrm{vL} \\ g = k_\mathrm{iLp}(i_\mathrm{Lref} - i_\mathrm{L}) + k_\mathrm{iLi}S_\mathrm{iL} \end{cases} \tag{3}$$

$$\frac{d\boldsymbol{x}_\mathrm{L}}{dt} = \boldsymbol{A}_\mathrm{L}\boldsymbol{x}_\mathrm{L} + \boldsymbol{B}_\mathrm{L}\boldsymbol{v}_\mathrm{F} \tag{4}$$

where $\boldsymbol{x}_{\mathrm{L}} = [\Delta i_{\mathrm{L}}, \Delta v_{\mathrm{L}}, \Delta S_{\mathrm{vL}}, \Delta S_{\mathrm{iL}}]^T$ and $\boldsymbol{v}_{\mathrm{F}} = [\Delta v_{\mathrm{F}}]^T$.

C. Small-Signal Modeling of the System

As shown in Fig. 1, the dc transmission lines are between the DGs and the CPLs. v_{DC} is the voltage of the common bus. R_{s} and L_{s} are the resistance and inductance of the transmission line at the source side, respectively. R_{F} and L_{F} are the resistance and inductance of the load-side transmission line, respectively. C_{DC} is the support capacitance of the common bus. The state-space model of the dc transmission lines is shown in (5), and its small-signal model is shown in (6). The length of the transmission lines from DGs 1, 2, and 3 to the common bus is l_{b1}, l_{b2}, and l_{b3}, separately

$$\begin{cases} C_{sn}\frac{dv_{on}}{dt} = (1-d_n)i_{\mathrm{b}n} - i_{on} \\ C_{\mathrm{DC}}\frac{dv_{\mathrm{DC}}}{dt} = i_{\mathrm{o1}} + i_{\mathrm{o2}} + i_{\mathrm{o3}} - i_{\mathrm{dc1}} - i_{\mathrm{dc2}} - i_{\mathrm{dc3}} \\ C_{\mathrm{F}n}\frac{dv_{\mathrm{F}n}}{dt} = i_{\mathrm{dc}n} - g_n i_{\mathrm{L}n} \\ L_{sn}\frac{di_{on}}{dt} = v_{on} - v_{\mathrm{DC}} - R_{sn}i_{on} \\ L_{\mathrm{F}n}\frac{di_{\mathrm{dc}n}}{dt} = v_{\mathrm{DC}} - v_{\mathrm{F}n} - R_{\mathrm{F}n}i_{\mathrm{dc}n} \end{cases} \tag{5}$$

$$\frac{d\boldsymbol{x}_{\mathrm{d123}}}{dt} = \boldsymbol{D}_{\mathrm{d123}}\boldsymbol{x}_{\mathrm{d123}} \tag{6}$$

where $\boldsymbol{x}_{\mathrm{d123}} = [\Delta v_{\mathrm{o1}}, \Delta v_{\mathrm{o2}}, \Delta v_{\mathrm{o3}}, \Delta v_{\mathrm{DC}}, \Delta v_{\mathrm{F1}}, \Delta v_{\mathrm{F2}}, \Delta v_{\mathrm{F3}}, \Delta i_{\mathrm{o1}}, \Delta i_{\mathrm{o2}}, \Delta i_{\mathrm{o3}}, \Delta i_{\mathrm{dc1}}, \Delta i_{\mathrm{dc2}}, \Delta i_{\mathrm{dc3}}]^T$.

In summary, the small-signal model of the system is

$$\frac{d\boldsymbol{x}_{\mathrm{sys}}}{dt} = \boldsymbol{A}_{\mathrm{sys}}\boldsymbol{x}_{\mathrm{sys}} \tag{7}$$

where $\boldsymbol{x}_{\mathrm{sys}} = [\boldsymbol{x}_{\mathrm{b}n}, \boldsymbol{x}_{\mathrm{L}n}, \boldsymbol{x}_{\mathrm{d123}}]^T$, $\boldsymbol{x}_{\mathrm{b}n}$ is the state variable of three DGs, $\boldsymbol{x}_{\mathrm{L}n}$ is the state variable of three CPLs, and $\boldsymbol{x}_{\mathrm{d123}}$ is the state variable of three transmission lines ($n = 1, 2, 3$). $\boldsymbol{A}_{\mathrm{sys}}$ is the state matrix of the system, as shown in (8). $\boldsymbol{A}_{\mathrm{b}n}$, $\boldsymbol{A}_{\mathrm{L}n}$, $\boldsymbol{B}_{\mathrm{b}n}$, $\boldsymbol{B}_{\mathrm{L}n}$, $\boldsymbol{C}_{\mathrm{b}n}$, $\boldsymbol{C}_{\mathrm{L}n}$, and $\boldsymbol{D}_{\mathrm{d123}}$ are shown in the Appendix. The subscript of the state variable in the equation is 0, which refers to the steady-state value. The subscripts are 1, 2, and 3 to distinguish the parameters of different DGs and CPLs

$$\boldsymbol{A}_{\mathrm{sys}} = \begin{bmatrix} \boldsymbol{A}_{\mathrm{b1}} & 0 & 0 & 0 & 0 & 0 & \boldsymbol{B}_{\mathrm{b1}} \\ 0 & \boldsymbol{A}_{\mathrm{b2}} & 0 & 0 & 0 & 0 & \boldsymbol{B}_{\mathrm{b2}} \\ 0 & 0 & \boldsymbol{A}_{\mathrm{b3}} & 0 & 0 & 0 & \boldsymbol{B}_{\mathrm{b3}} \\ 0 & 0 & 0 & \boldsymbol{A}_{\mathrm{L1}} & 0 & 0 & \boldsymbol{B}_{\mathrm{L1}} \\ 0 & 0 & 0 & 0 & \boldsymbol{A}_{\mathrm{L2}} & 0 & \boldsymbol{B}_{\mathrm{L2}} \\ 0 & 0 & 0 & 0 & 0 & \boldsymbol{A}_{\mathrm{L3}} & \boldsymbol{B}_{\mathrm{L3}} \\ \boldsymbol{C}_{\mathrm{b1}} & \boldsymbol{C}_{\mathrm{b2}} & \boldsymbol{C}_{\mathrm{b3}} & \boldsymbol{C}_{\mathrm{L1}} & \boldsymbol{C}_{\mathrm{L2}} & \boldsymbol{C}_{\mathrm{L3}} & \boldsymbol{D}_{\mathrm{d123}} \end{bmatrix}. \tag{8}$$

D. Oscillation Mode Identification

The system parameters of the MSML dc microgrid are shown in Table I. The parameters are defined as the standard values. Substituting the parameters into $\boldsymbol{A}_{\mathrm{sys}}$ to calculate the eigenvalues, it can be seen that the system has 34 eigenvalues, and the distribution of eigenvalues is shown in Fig. 4. The system has 12 groups of oscillation modes. The influence degree of state variables on modes is decoupled by the participation factor method. According to Figs. 4 and 5, the oscillation modes of system are identified and categorized into three colored groups.

TABLE I
SYSTEM PARAMETERS

	Parameter	Value	Parameter	Value
DGs	$v_{\mathrm{b}n}$	120 V	$C_{\mathrm{virb}n}$	0.05
	$R_{\mathrm{b}n}$	0.001 Ω	$K_{\mathrm{droop}n}$	1
	$L_{\mathrm{b}n}$	500 μH	$k_{\mathrm{p}n}$	0.0005
	C_{sn}	0.0055 F	k_{in}	0.1
	$v_{\mathrm{o}N}$	800 V	T	0.05
CPLs	$v_{\mathrm{L}n}$	400 V	$k_{\mathrm{vLp}n}$	10
	$R_{\mathrm{L}n}$	0.1 Ω	$k_{\mathrm{vLi}n}$	100
	$L_{\mathrm{L}n}$	2 mH	$k_{\mathrm{iLp}n}$	0.001
	$C_{\mathrm{L}n}$	0.001 F	$k_{\mathrm{iLi}n}$	0.05
	$C_{\mathrm{F}n}$	0.0055 F	$P_{\mathrm{L}n}$	10 kW
DC transmission lines	v_{DC}	800 V	C_{DC}	0.0055 F
	$R_{\mathrm{s}1}$	0.003/2 Ω	$R_{\mathrm{F}1}$	0.3/2 Ω
	$L_{\mathrm{s}1}$	20/2 μH	$L_{\mathrm{F}1}$	2/2 μH
	$R_{\mathrm{s}2}$	0.003/3 Ω	$R_{\mathrm{F}2}$	0.3/3 Ω
	$L_{\mathrm{s}2}$	20/3 μH	$L_{\mathrm{F}2}$	2/3 μH
	$R_{\mathrm{s}3}$	0.003/6 Ω	$R_{\mathrm{F}3}$	0.3/6 Ω
	$L_{\mathrm{s}3}$	20/6 μH	$L_{\mathrm{F}3}$	2/6 μH

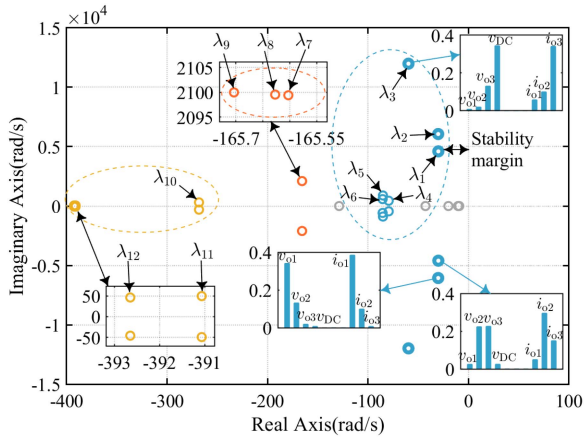

Fig. 4. Analysis of system eigenvalue and participation factor.

1) λ_1–λ_6 are mainly associated with the state variables of voltage and current of the source-side and load-side lines. The blue group is related to the overall coupling.
2) λ_7–λ_9 are associated only with state variables inside the CPLs. The orange group represents the coupling of CPLs.
3) λ_{10}–λ_{12} are mainly associated with state variables inside the DGs. The yellow group denotes the internal coupling of DGs. In addition, the dominant modes λ_1–λ_3 under the parameters in Table I are related to the voltage and current changes of the source-side line.

The matrix $\boldsymbol{A}_{\mathrm{sys}}$ exhibits ten real eigenvalues (gray group), which are all negative and not sensitive to the system parameters and the operating point. Therefore, they are not of significance with respect to the system dynamics and are not further discussed [16], [24]. In this article, the stability margin of the system is expressed by the distance between the real part of the maximum oscillation mode and the imaginary axis.

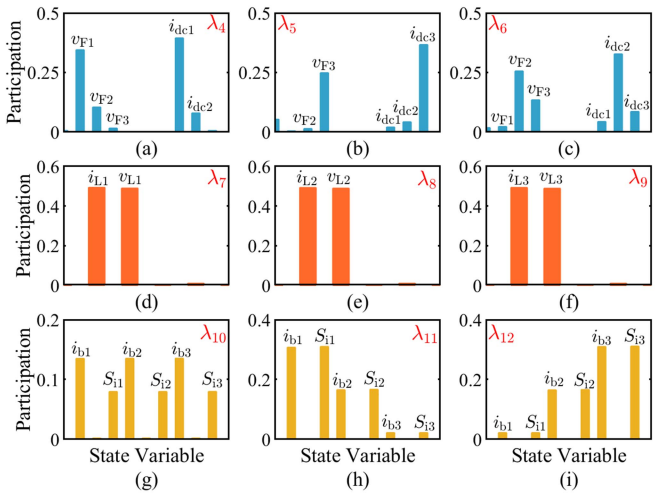

Fig. 5. Participation factor of oscillation modes. (a) Analysis of λ_4. (b) Analysis of λ_5. (c) Analysis of λ_6. (d) Analysis of λ_7. (e) Analysis of λ_8. (f) Analysis of λ_9. (g) Analysis of λ_{10}. (h) Analysis of λ_{11}. (i) Analysis of λ_{12}.

III. Stability Analysis Considering Homogeneous Parameter Interaction

A. Variation of Transmission Lines

For a uniform network where the impedance per unit length of each line segment is equal, the equivalent line impedance is

$$Z_{bn} = \left(\sum_{n=1}^{3} R_{sn} + j\omega \sum_{n=1}^{3} L_{sn}\right) l_{bn}. \tag{9}$$

The total length of the transmission lines at the source side is set to per unit value . That is, l_{b1}+l_{b2}+l_{b3} = 1 p.u. The stability margin under the change of line parameters is shown in Fig. 6. As shown in Fig. 6(b), the stability margin of the system is minimum when it approaches zero along the direction of $l_{b2} = l_{b1}$. The TSOL means $l_{b3} \gg l_{b2}$, l_{b1}, and the "one long" of l_{b3} is more than ten times that of the "two short" of l_{b2} and l_{b1}. The more asymmetrical along the $l_{b2} > l_{b1}$ direction, the greater the stability margin of the system. The TLOS means l_{b3}, $l_{b2} \gg l_{b1}$, and the "two long" of l_{b3}, l_{b2} is more than ten times that of the "one short" of l_{b1}. The analysis is as follows.

The root locus of the dominant modes in the two directions $l_{b2} = l_{b1}$ and $l_{b2} > l_{b1}$ is shown in Fig. 7. As shown in Fig. 7(a), with the gradual decrease of l_{b2} and l_{b1}, dominant modes λ_1 and λ_2 get closer. When close enough, the two sets of frequencies are superimposed on each other. Subsequently, the dominant modes λ_1 and λ_2 repel each other. It can be seen that, due to the symmetry of l_{b2} and l_{b1}, the dominant modes λ_1 and λ_2 interact with each other. As l_{b2} and l_{b1} become smaller and smaller, they will repel each other along the real axis. As shown in Fig. 7(b), along the direction $l_{b2} > l_{b1}$, the imaginary parts of dominant modes λ_1 and λ_2 keep moving away. Besides, they have no intersection and are far away from the imaginary axis. It can be seen that as the asymmetry of l_{b2} and l_{b1} increases, the interaction between dominant modes λ_1 and λ_2 becomes weaker.

Then, the participation factor of the dominant modes in two directions $l_{b2} = l_{b1}$ and $l_{b2} > l_{b1}$ of Fig. 6(b) is analyzed, as

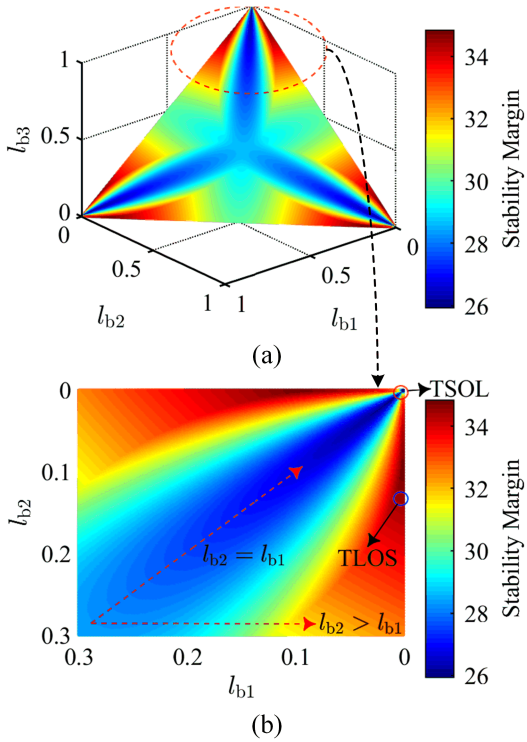

Fig. 6. Stability margin. (a) Variation of three transmission lines when l_{b1}+l_{b2}+l_{b3} = 1 p.u. (b) Partial enlargement of (a).

shown in Fig. 8. In the direction of $l_{b2} = l_{b1}$, Fig. 8(a)–(c) illustrates that two short lines corresponding to state variables Δv_{o1}, Δv_{o2}, Δi_{o1}, and Δi_{o2} are coupled between the dominant modes λ_2 and λ_3, which indicates that the dominant modes have identical characteristics. This results in the mutual repulsion of modes λ_2 and λ_3 in the complex plane shown in Fig. 7(a). The interesting phenomenon is similar to "like charges repel each other." The reason for the decrease in stability margin in TSOL transmission is the repulsion of the same dominant modes. It can be seen from Fig. 8(d)–(f) that the state variables of the three lines gradually decouple from the three dominant modes along the direction of $l_{b2} > l_{b1}$. The similarities between the three modes gradually weakens and the difference increases. By observing Fig. 7(b), it can be found that the real part of the three dominant modes is gradually approaching, which indicates that the modes of different properties attract each other. The interesting phenomenon is similar to "unlike charges attract each other." Therefore, under TLOS transmission with increased stability margin, the state variables of voltage and current in the dominant modes will be decoupled, resulting in attraction between highly different modes.

Next, the applicability of the above conclusions is verified under different parameters and output power of the DGs. First of all, two sets of different virtual inertia coefficients are taken under other parameters are standard. The stability margin under the change of three transmission lines is analyzed, as shown in Fig. 9(a) and (b) . Two groups of different droop coefficients are taken to represent the difference in the output power of the DGs. The above analysis is repeated, and the results are shown in Fig. 9(c) and (d). As can be seen from Fig. 9(a)–(d),

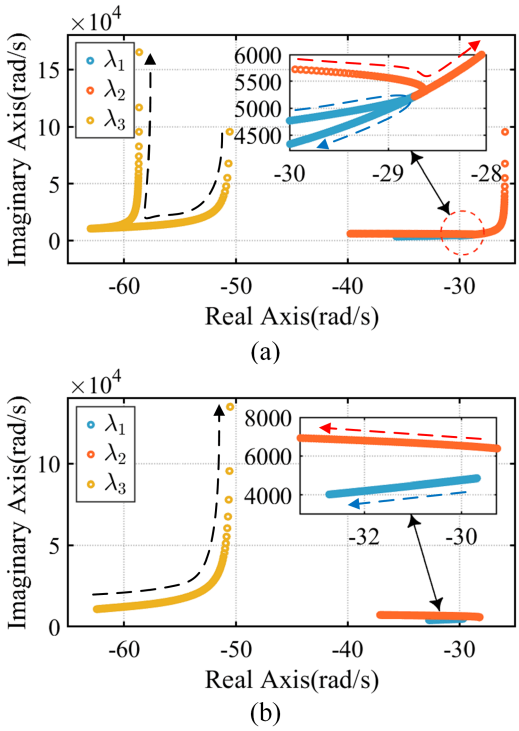

Fig. 7. Root locus of the dominant modes. (a) Variation of direction along $l_{b2} = l_{b1}$ in Fig. 6(b). (b) Variation of direction along $l_{b2} > l_{b1}$ in Fig. 6(b).

the conclusion that " stability margin is larger when the three lines at the source side are under TLOS transmission than TSOL transmission" is valid. Moreover, from the analysis of participation factor in Fig. 5, modes 4–6 affected by changing the parameters of load-side line are not the dominant modes. The influence of these parameters on the stability margin can be ignored.

B. Variation of Multisource and Multiload

Under the same ideal condition, the total power of the three CPLs remains constant. The analysis of eigenvalue and participation factor under multisource parallel is shown in Fig. 10. In Fig. 10(a), with the increase of DGs, the stability margin increases gradually. It is explained as follows.

Assume that the equivalent impedance of the source side is v_o/i_o under one DG connection. All the variables here are steady-state values. When n DGs are connected, the total equivalent impedance at the source side is v_o'/i_o'. And the current of n DGs is reduced to i_o'/n after being equally divided, so that v_o' rises slightly due to characteristics of droop control, that is, $v_o' > v_o$. Since the load power remains unchanged, there is $i_o' < i_o$, so there is $v_o'/i_o' > v_o/i_o$, which is obvious that the source-side impedance increases after multisource in parallel. The phenomenon that the output impedance increases with the increase of DGs is called the IAE.

From the participation factor analysis of the dominant modes, the state variable $\Delta r_{on} = \Delta v_{on}/\Delta i_{on}$ of the output impedance is assumed according to Figs. 4 and 10(a). The impedance participation for the dominant mode λ_i is the parallel form of Δr_{on}. When there are multiple dominant modes, the participation ΔR_j of the output impedance is the sum of multiple λ_i, where j represents the number of dominant modes. The expression of ΔR_j is shown in (10). Fig. 10(b) shows the multisource output impedance participation, which can be seen as $\Delta R_1 < \Delta R_2 < \Delta R_3$. This also confirms the results of IAE from the side. The IAE makes the dominant modes of the system far away from the imaginary axis and improves the system stability, which verifies the situation in Fig. 10(a)

$$\Delta R_n = \sum_{i=1}^{j} \lambda_i \left(r_{o1}//\ldots//r_{on}\right) = \sum_{i=1}^{j} \lambda_i \left(\frac{\Delta v_{o1}}{\Delta i_{o1}}//\ldots//\frac{\Delta v_{on}}{\Delta i_{on}}\right). \quad (10)$$

In addition, when the number of DGs is three, Fig. 11 shows the system eigenvalue under the condition of increasing the same CPL. It can be found that dominant modes λ_1, λ_2, and λ_3 gradually approach the imaginary axis, and the stability margin decreases. The results show that increasing CPLs only causes the movement of the dominant modes by affecting the output power of the DGs, but does not affect the change of the participation factor in the dominant modes. This can be seen from the result of substituting (10) in Fig. 11, which does not produce the IAE.

IV. Interaction-Rule-Based Optimization Method for Controller Parameters

A. Dynamic Analysis of Virtual Inertia Coefficient and Droop Coefficient

Under the standard parameters, the influence of virtual inertia coefficient and droop coefficient of the three DGs on the stability margin is studied. On this basis, the stability margin of the two parameters is shown in Fig. 12. When the two kinds of parameters of each DG become smaller, the real part of the dominant mode is smaller, and thus, the system has a larger stability margin. The analysis is as follows.

According to (1), the voltage–current equation related to the control parameters can be obtained. It can be seen that the smaller virtual inertia coefficient and droop coefficient, the larger the corresponding equivalent impedance of the DG. The dominant mode of the system is far away from the imaginary axis, the system has greater damping, and the system is more stable. Moreover, the minimum value of the virtual inertia coefficient can be zero, in which case the virtual inertia control does not participate in regulating the dynamic behavior of dc bus voltage. As the droop coefficient decreases, the stability margin will increase. However, the voltage of the dc bus will drop. While pursuing the maximum stability margin, it is necessary to consider that the deviation of voltage bus is within 5%, so the value of droop coefficient cannot be zero.

Fig. 13 shows the dynamic characteristics of the dominant mode under the variation of droop coefficient. When the droop coefficient is smaller, the damping ratio of the dominant mode will increase and the overshoot of the dominant mode will decrease. This shows that the smaller the droop coefficient, the better the dynamic behavior of the system.

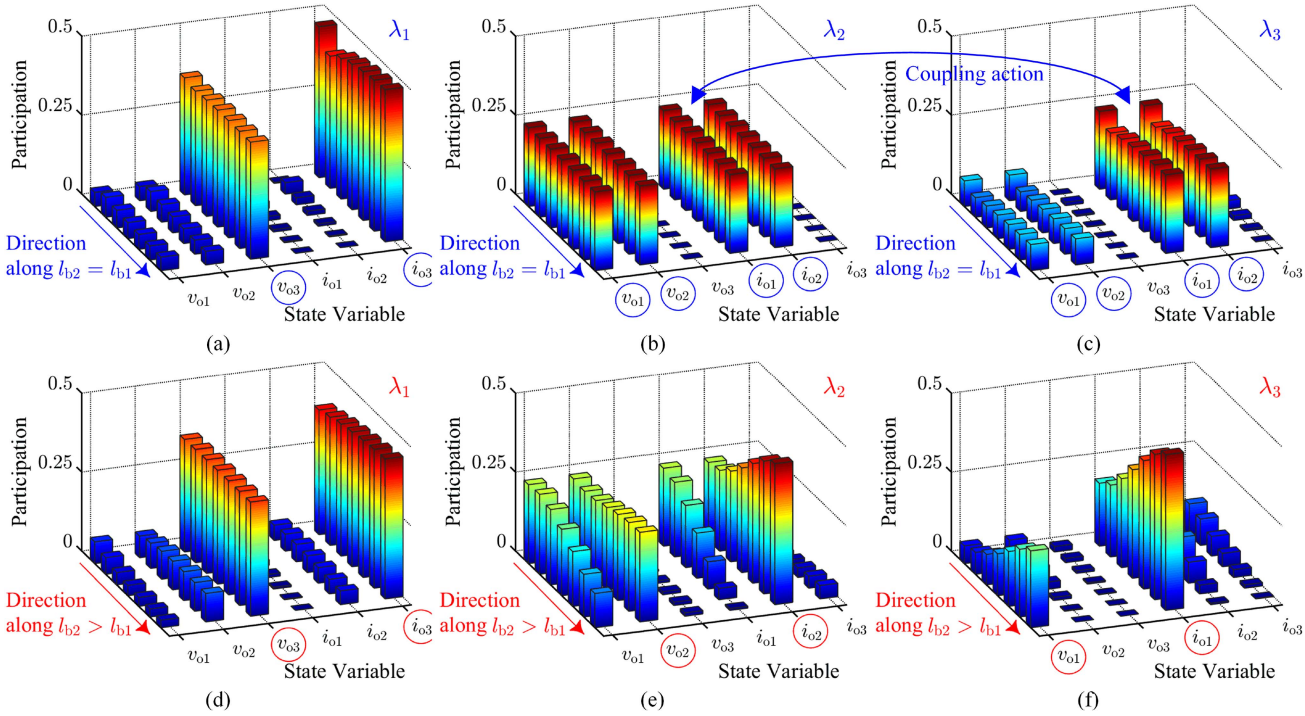

Fig. 8. Participation factor analysis of dominant modes. (a) λ_1 changes in the direction of $l_{b2} = l_{b1}$. (b) λ_2 changes in the direction of $l_{b2} = l_{b1}$. (c) λ_3 changes in the direction of $l_{b2} = l_{b1}$. (d) λ_1 changes in the direction of $l_{b2} > l_{b1}$. (e) λ_2 changes in the direction of $l_{b2} > l_{b1}$. (f) λ_3 changes in the direction of $l_{b2} > l_{b1}$.

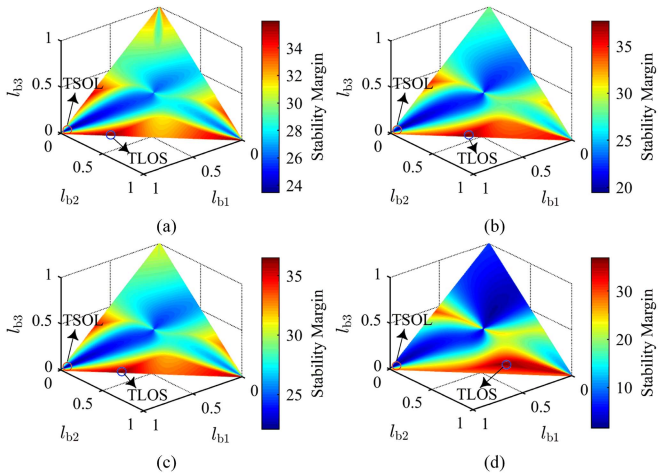

Fig. 9. Different parameters and output power of the DGs. (a) $C_{\text{virb1}} = 0.04$, $C_{\text{virb2}} = 0.05$, $C_{\text{virb3}} = 0.06$. (b) $C_{\text{virb1}} = 0.025$, $C_{\text{virb2}} = 0.5$, $C_{\text{virb3}} = 0.075$. (c) $K_{\text{droop1}} = 0.9$, $K_{\text{droop2}} = 1$, $K_{\text{droop3}} = 1.1$. (d) $K_{\text{droop1}} = 0.5$, $K_{\text{droop2}} = 1$, $K_{\text{droop3}} = 1.5$.

B. Interactive Stability Analysis of Virtual Inertia Coefficient and Droop Coefficient

The influence law of the dynamic interaction between the margin of virtual inertia coefficient and droop coefficient of three DGs on the system operation is studied. $C_{\text{virb}n}$ margin is expressed as the value of the corresponding $C_{\text{virb}n}$ when the system is in critical stability. The significance of this value is the maximum ability to improve the system inertia. Set K_{droop2} and K_{droop3} of the second and third DGs as 0.5 and 1, and other parameters are standard values except K_{droop1} and $C_{\text{virb}n}$. In order to ensure system stability, the relationship between $C_{\text{virb}n}$ margin of the three DGs and K_{droop1} of the first DG is shown in Fig. 14(a). When K_{droop1} gradually increases, C_{virb1} margin of the first DG decreases, while C_{virb2} and C_{virb3} margins of the second and third DGs increase. When K_{droop1} increases to a certain extent, C_{virb2} and C_{virb3} margins begin to become smaller. The reason is as follows.

Take points (c)–(h) in Fig. 14(a) and use Fig. 14(c)–(h) to show how $C_{\text{virb}n}$ margin is generated by the root locus. Under constant load power, it can be seen from Fig. 2 that the droop coefficient is positively correlated with the output power of the DG. According to Fig. 14(b), as K_{droop1} increases, dominant mode λ_1 moves to the right, while dominant modes λ_2 and λ_3 move to the left. Fig. 14(c) and (f) shows that C_{virb1} margin is mainly determined by the dominant mode λ_1. As the output power of the first DG increases and the dominant mode λ_1 approaches the imaginary axis, the virtual inertia of this DG will gradually decrease. Fig. 14(d) and (e) shows that C_{virb2} and C_{virb3} margins are mainly determined by the dominant mode λ_2. In addition, since $K_{\text{droop2}} < K_{\text{droop3}}$, the second DG with low output power will cause dominant mode λ_2 to move more slowly. As the output power of the second and third DGs decreases, the dominant mode λ_2 is far away from the imaginary axis, and the virtual inertia of DGs will gradually increase.

When the output power of the first DG is large enough, the dominant mode λ_1 is very close to the imaginary axis. As can be seen from Fig. 14(g) and (h), C_{virb2} and C_{virb3} margins become related to the dominant mode λ_1. At this point, the dominant mode λ_1 reaches the imaginary axis faster than the

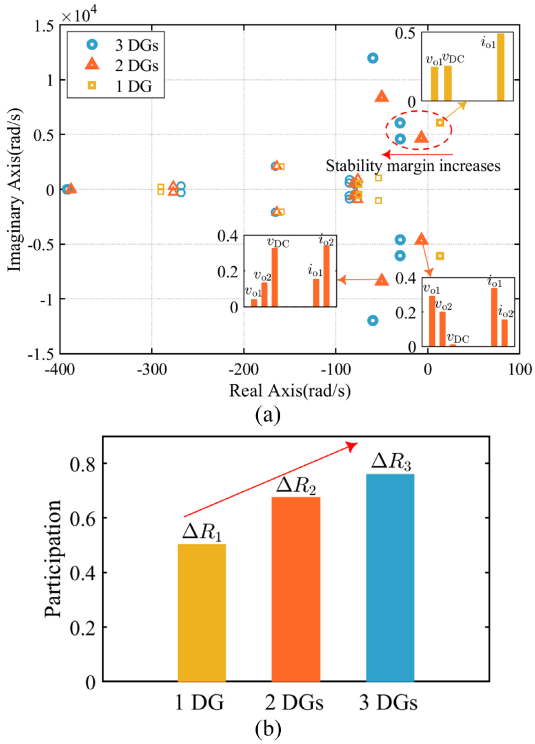

Fig. 10. Analysis of multisource in parallel. (a) Analysis of eigenvalue and participation factor of one and two DGs. (b) Analysis of output impedance participation factor.

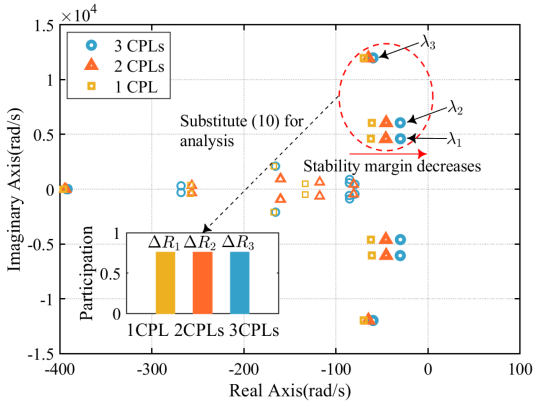

Fig. 11. Analysis of multiload in parallel.

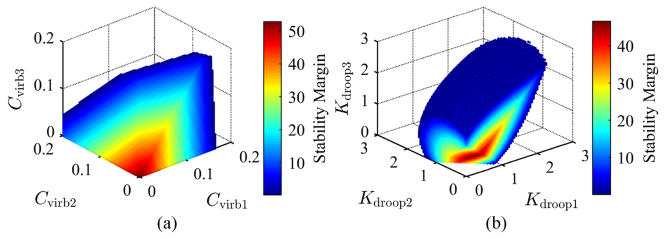

Fig. 12. Stability margin. (a) Virtual inertia coefficient. (b) Droop coefficient.

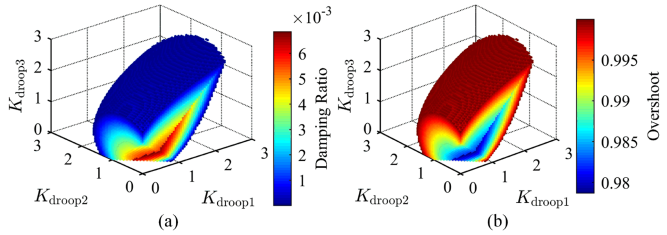

Fig. 13. Dynamic characteristics of the dominant mode. (a) Damping ratio. (b) Overshoot.

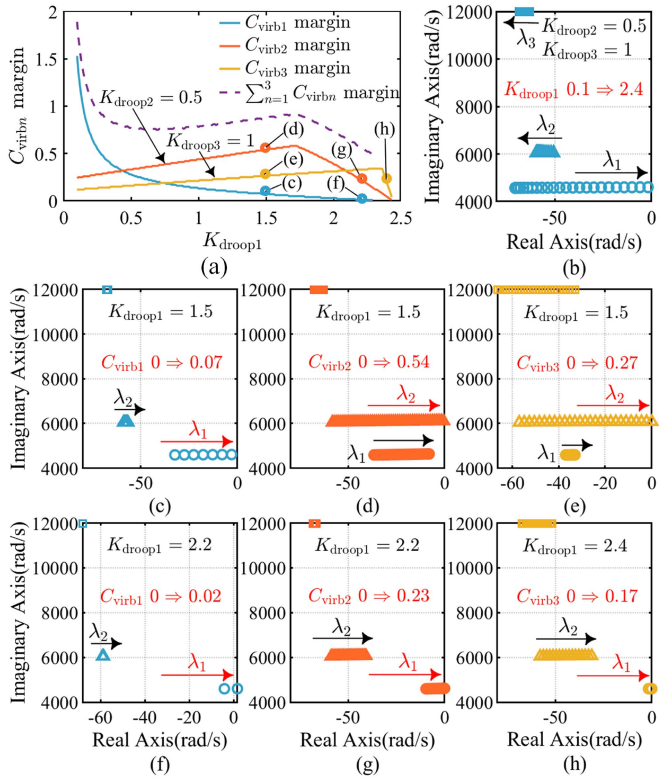

Fig. 14. Interactive stability analysis. (a) Interaction between C_{virbn} and K_{droopn}. (b) When $K_{droop2} = 0.5$ and $K_{droop3} = 1$, K_{droop1} changes the corresponding root locus. (c) When $K_{droop1} = 1.5$, C_{virb1} changes the corresponding root locus. (d) When $K_{droop1} = 1.5$, the margin of C_{virb2}. (e) When $K_{droop1} = 1.5$, the margin of C_{virb3}. (f) When $K_{droop1} = 2.2$, the margin of C_{virb1}. (g) When $K_{droop1} = 2.2$, the margin of C_{virb2}. (h) When $K_{droop1} = 2.4$, the margin of C_{virb3}.

dominant mode λ_2, so the virtual inertia of second and third DGs goes down. In addition, Fig. 14(a) shows that under voltage constraints, the maximum sum of C_{virbn} margin occurs when K_{droop1} is minimum. This phenomenon is one of the rules for optimizing parameters.

C. Interaction-Rule-Based Optimization Method

It is necessary to improve the overall stability of the system and make multisource have greater inertial support ability. Considering the interaction of control parameters, the rule-based optimization method of virtual inertia coefficient and droop

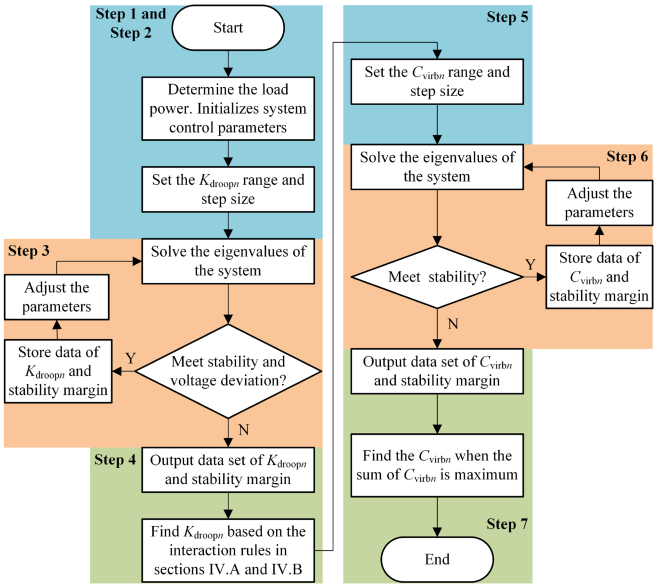

Fig. 15. Flowchart for interaction-rule-based optimization.

coefficient of each DG is proposed. The process of optimization is shown in Fig. 15. The specific steps are as follows.

1) *Step 1:* Determine the load power and initialize the control parameters (set $K_{\text{droop}n}$ to the standard value and $C_{\text{virb}n}$ to zero).
2) *Step 2:* The value range and calculation step size of the droop coefficients of each DG are set.
3) *Step 3:* Substitute the parameters into (8) to solve the eigenvalues of the system. Determine whether the system stability and the deviation of bus voltage meet the requirements. If yes, store the data of the droop coefficients and stability margin at this time, and adjust the droop coefficients according to the step size. Repeat step 3. Otherwise, go to Step 4.
4) *Step 4:* The dataset of droop coefficient and stability margin are output. According to Section IV-A, when the deviation of bus voltage is less than 5%, the smaller the droop coefficient is, the larger the stability margin is, and the droop coefficient has better dynamic characteristics. According to Section IV-B, the smaller droop coefficient of one DG is conducive to inertia output. Considering a large stability margin and a small droop coefficient, determine the droop coefficients and keep the value unchanged.
5) *Step 5:* The value range and calculation step size of the virtual inertia coefficient of each DG are set.
6) *Step 6:* Substitute the parameters into (8) to solve the eigenvalues of the system. Check whether the system stability meets the requirements. If yes, store the data of the virtual inertia coefficients at this time and adjust the coefficients according to the step size. Repeat step 6. Otherwise, go to Step 7.
7) *Step 7:* Output dataset of the virtual inertia coefficient. When the sum of the virtual inertia coefficient of each DG is maximum, the value of the virtual inertia coefficient is determined.

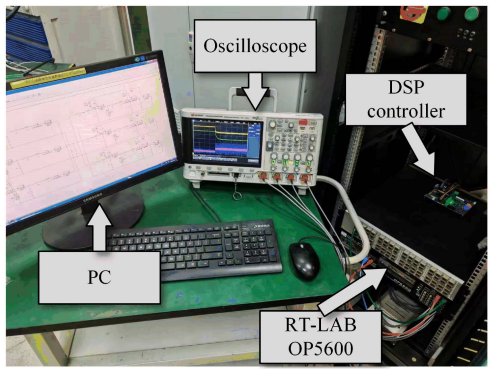

Fig. 16. Hardware-in-the-loop experimental platform.

According to the above steps, the control parameters of the system are optimized. Under the load power of 51 kW, the other parameters are standard values except virtual inertia coefficient and droop coefficient. According to Step 4, the droop coefficients of the first, second, and third DGs are 0.8, 0.15, and 1, respectively. According to Step 7, the maximum sum of the virtual inertia coefficients of all DGs is 0.37, and the corresponding virtual inertia coefficients of the DGs are 0.04, 0.3, and 0.03, respectively.

V. Experiment Verification

To verify the correctness of the above theoretical analysis, a hardware-in-the-loop experimental platform for the MSML system based on RT-LAB and DSP F28335 controller is built, as shown in Fig. 16. Information of experimental cases is shown in Table II. Four experiments are carried out, including nine cases.

A. Experiment I: The Parameters of Source-Side Lines

Case 1 adopts standard line parameters at the source side, and Case 2 sets TLOS lines at the source side. When switching from Case 1 to Case 2, the experimental waveforms of the bus voltage and power are shown in Fig. 17. Under Case 1, the bus voltage and power oscillate, and the main oscillation frequencies are around 710 and 900 Hz, which are basically consistent with the theoretical values of 732 and 965 Hz in Fig. 18. Compared with Case 1, the bus voltage is in stable operation under Case 2. The oscillation amplitude near 710 Hz decreases from 0.35 to 0.1 V. Therefore, the experimental results verify that the system has greater stability margin when the three lines on the source side are in TLOS states.

B. Experiment II: Multisource in Parallel

Case 3 refers to the connection of one DG and Case 4 refers to the connection of two DGs. The total power of the three loads initially is 9 kW. When $t = 2$ s, the power suddenly increases to 30 kW. The experimental waveforms of the bus voltage and power under Cases 3 and 4 are shown in Fig. 19(a). After the power increases, the bus voltage and power oscillate under Case 3. The main oscillation frequency is near 880 Hz, the oscillation

TABLE II
SPECIFIC CASES

Experiment	Case	Parameter	Total load power	System stability	Theoretical value of frequency	Experimental value of frequency	Oscillation amplitude	Buffer time of voltage
I	1	Standard values: l_{b1}, l_{b2}, l_{b3} = 1/2, 1/3, 1/6	51 kW	No	732 Hz 965 Hz	710 Hz 900 Hz	0.35 V 0.2 V	/
	2	TLOS: l_{b1}, l_{b2}, l_{b3} = 0.01, 0.14, 0.85	51 kW	Yes	/	/	/	/
II	3	one DG	30 kW	No	869 Hz	880 Hz	0.9 V	/
	4	two DGs	30 kW	Yes	/	/	/	/
	5	two DGs	36 kW	No	742 Hz	730 Hz	0.85 V	/
	6	three DGs	36 kW	Yes	/	/	/	/
III	7	Not optimized parameters: K_{droop1} = 1, K_{droop2} = 1, K_{droop3} = 1, C_{virb1} = 0.05, C_{virb2} = 0.05, C_{virb3} = 0.05	51 kW	No	Same Case 1	Same Case 1	Same Case 1	0.3 s
	8	Interaction rule-based optimization: K_{droop1} = 0.8, K_{droop2} = 0.15, K_{droop3} = 1, C_{virb1} = 0.04, C_{virb2} = 0.3, C_{virb3} = 0.03	51 kW	Yes	/	/	/	0.7 s
IV	9	Parameters obtained by PSO: K_{droop1} = 1, K_{droop2} = 0.16, K_{droop3} = 0.52, C_{virb1} = 0.01, C_{virb2} = 0.01, C_{virb3} = 0.18	51 kW	Yes	/	/	/	0.4 s

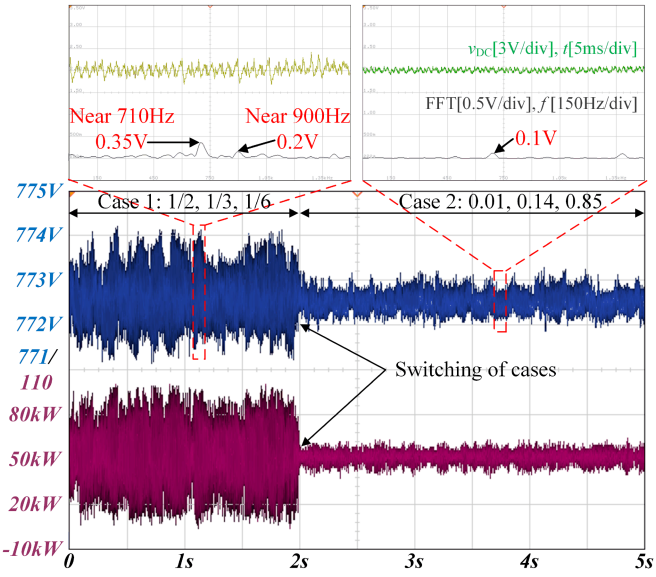

Fig. 17. Waveforms of bus voltage and power in experiment I.

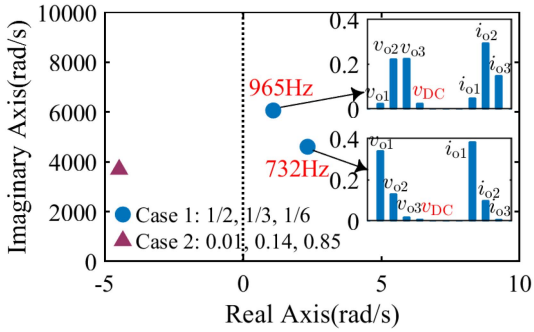

Fig. 18. Eigenvalue analysis of different line parameters.

amplitude is 0.9 V, and the bus voltage drops to 746 V, which does not meet the requirement of 5% voltage deviation.

Compared with Case 3, the bus voltage under Case 4 is stable after the sudden increase in power. The bus voltage drops to 778 V, with a small drop. The oscillation amplitude of the bus voltage near 880 Hz decreases from 0.9 V to almost nothing. The reasons are as follows: Since the source-side output impedance value 746/40.2 = 18.6 under Case 3 is less than the output impedance value 778/38.5 = 20.2 under Case 4, in which 40.2 and 38.5 A are bus current under two cases, respectively, the system damping under Case 3 is less than that under Case 4, which makes Case 3 easy to cause system oscillation.

Then, the experimental waveforms of the bus voltage and power under Cases 5 and 6 are shown in Fig. 19(b). Cases 5 and 6 represent connecting two DGs and three DGs, respectively. After t = 2 s, the system loses stability under Case 5, and the oscillation amplitude near 730 Hz is 0.85 V. The bus voltage and power under Case 6 are stable, and the oscillation amplitude near 730 Hz drops to 0.1 V. The reason is that the steady-state value of bus voltage under Case 5 is 775 V, which is less than 783 V under Case 6. At this time, the bus current of the two cases is 46.4 and 45.9 A, respectively. As the number of DGs increases, the bus voltage rises slightly due to the droop characteristics, and the total load power remains unchanged, resulting in a small drop in bus current. Therefore, the output impedance of the former is smaller than that of the latter, which reduces the system damping of the former and makes it easy to oscillate.

The above experimental results show that with the increase in the number of sources, the output impedance of the source side becomes larger, resulting in the IAE, which can make the system more stable. It is consistent with the eigenvalue analysis in Fig. 20 to jointly verify the correctness of the theoretical analysis.

C. Experiment III: Interaction-Rule-Based Optimization

Case 7 is the standard values before optimizing the control parameters. When the total load power is 51 kW, Case 8 is the result of interaction-rule-based optimization. The experimental waveforms of bus voltage and power under Cases 7 and 8 are

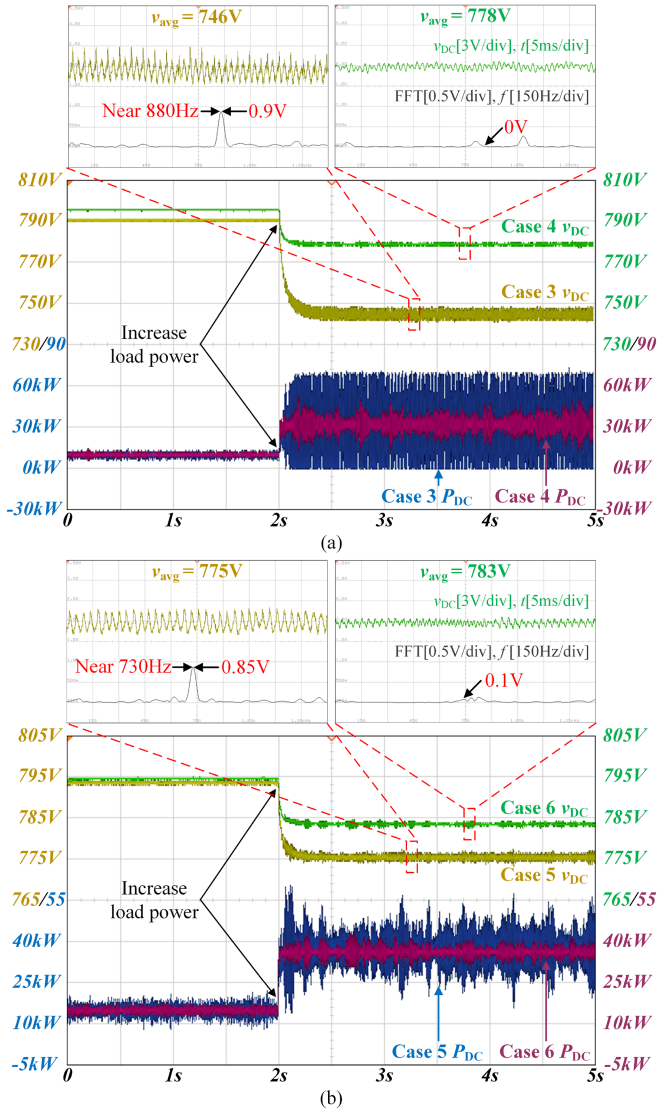

Fig. 19. Waveforms of bus voltage and power in experiment II. (a) Comparison between one DG and two DGs. (b) Comparison between two DGs and three DGs.

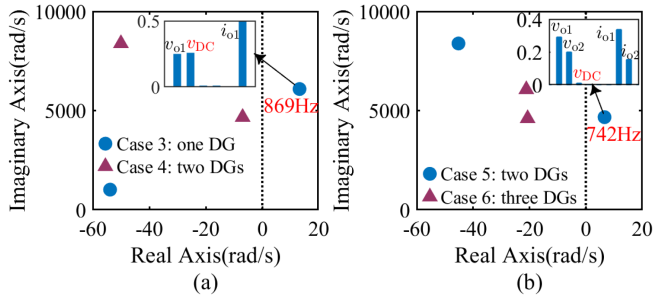

Fig. 20. Eigenvalue analysis of experiment II. (a) Comparison between one DG and two DGs. (b) Comparison between two DGs and three DGs.

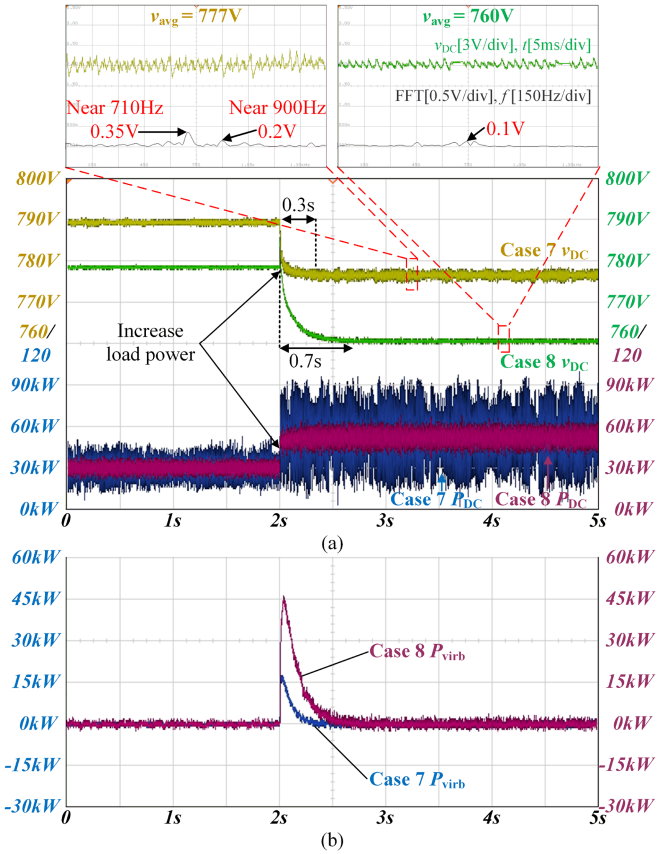

Fig. 21. Results of experiment III. (a) Waveforms of bus voltage and power before and after optimization. (b) Comparison of virtual inertia.

shown in Fig. 21(a). After $t = 2$ s, the stability and dynamics under Case 7 are poor, because the control parameters are not optimized at this time, and the damping and inertial support capacity of the system are small.

In the steady state after the sudden increase of load power, the oscillation amplitude under Case 8 near 710 Hz is reduced from 0.35 to 0.1 V compared with that under Case 7, indicating that the bus voltage and power under Case 8 are relatively more stable. The reason is that the droop coefficients corresponding to Case 8 are small, resulting in large system damping and better system stability. In the dynamic process after the increase of load power, the time of buffer bus voltage under Cases 7 and 8 is 0.3 and 0.7 s, respectively, which indicates that Case 8 has greater inertial capacity. Fig. 21(b) shows that the output virtual inertia of Case 8 is larger than that of Case 7. The reason is that the sum of virtual inertia coefficient corresponding to Case 8 is large, that is, $0.37 > 0.15$, which makes the sources provide more virtual inertia to buffer the sudden change of bus voltage.

D. Experiment IV: Comparison of Optimization Methods

The proposed method is compared with the optimization algorithm based on artificial intelligence. As referred to [34], the objective function is established with the sum of the virtual inertia coefficients, and the fitness function is established considering the stability constraint and the voltage constraint. The PSO is used to obtain the parameters of Case 9 in Table II. The results of Cases 8 and 9 are compared, and the experimental waveform is shown in Fig. 22. In Cases 8 and 9, the time to buffer the mutation is 0.7 and 0.4 s, respectively. Because the total number of virtual inertia coefficients is $0.37 > 0.2$, the power output of the inertia of Case 8 is greater than that of

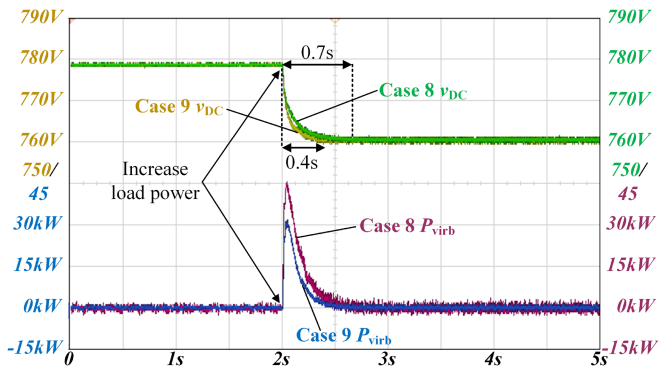

Fig. 22. Waveforms of bus voltage and virtual inertia in experiment IV.

Case 9. In addition, the bus voltage is stable in both the cases. It is shown that the proposed method is more effective by considering the interaction rules of parameters than the PSO method.

VI. Conclusion

This article analyzes the interaction stability and proposes an interaction-rule-based optimization method for the controller parameters in the MSML dc microgrid. Main conclusions are listed as follows.

1) In a three-source system, the system stability of TLOS transmission lines is better than that of TSOL transmission lines. When the coupling of state variables in the dominant modes becomes strong, the stability margin is much more likely to decrease. Generally, a weak coupling of state variables in the dominant modes is conducive to system stability.
2) The influence mechanism of sources on system stability is uniformly summarized. When the total system power is constant, it shows that the IAE generated by the increase of the sources can improve the stability margin. In addition, increasing the loads will cause the system instability and will not produce IAE.
3) Based on the coupling interaction analysis between the virtual inertia coefficient and the droop coefficient, an interaction-rule-based optimization method is proposed for control parameters, which improves the stability and inertia of the system. It provides a new idea for the optimization of control parameters.

Appendix

$$\boldsymbol{A}_{\mathrm{bn}}=\begin{bmatrix}-\frac{R_{\mathrm{bn}}+k_{\mathrm{pn}}v_{\mathrm{o0}}}{L_{\mathrm{bn}}} & -\frac{k_{\mathrm{pn}}C_{\mathrm{virbn}}v_{\mathrm{o0}}}{2TL_{\mathrm{bn}}v_{\mathrm{bn}}} & \frac{k_{in}v_{\mathrm{o0}}}{L_{\mathrm{bn}}}\\ 0 & -\frac{1}{T} & 0\\ -1 & -\frac{C_{\mathrm{virbn}}}{2Tv_{\mathrm{bn}}} & 0\end{bmatrix} \tag{A1}$$

$$\boldsymbol{B}_{\mathrm{bn}}=\begin{bmatrix}\frac{1}{L_{\mathrm{bn}}}\left(d_0-1+\frac{k_{\mathrm{pn}}K_{\mathrm{droopn}}v_{\mathrm{oN}}v_{\mathrm{o0}}}{v_{\mathrm{bn}}}-\frac{2k_{\mathrm{pn}}K_{\mathrm{droopn}}v_{\mathrm{o0}}^2}{v_{\mathrm{bn}}}-\frac{k_{\mathrm{pn}}C_{\mathrm{virbn}}v_{\mathrm{o0}}^2}{Tv_{\mathrm{bn}}}\right)\\ -\frac{2v_{\mathrm{o0}}}{T}\\ \frac{K_{\mathrm{droopn}}v_{\mathrm{oN}}}{v_{\mathrm{bn}}}-\frac{2K_{\mathrm{droopn}}v_{\mathrm{o0}}}{v_{\mathrm{bn}}}-\frac{C_{\mathrm{virbn}}v_{\mathrm{o0}}}{Tv_{\mathrm{bn}}}\end{bmatrix} \tag{A2}$$

$$\boldsymbol{A}_{\mathrm{Ln}}=\begin{bmatrix}-\frac{k_{\mathrm{iLpn}}v_{\mathrm{F0}}+R_{\mathrm{Ln}}}{L_{\mathrm{Ln}}} & \frac{1}{C_{\mathrm{Ln}}} & 0 & -1\\ -\frac{k_{\mathrm{iLpn}}k_{\mathrm{vLpn}}v_{\mathrm{F0}}+1}{L_{\mathrm{Ln}}} & \frac{P_{\mathrm{Ln}}}{C_{\mathrm{Ln}}v_{\mathrm{L0}}^2} & -1 & -k_{\mathrm{vLpn}}\\ \frac{k_{\mathrm{iLpn}}k_{\mathrm{vLin}}v_{\mathrm{F0}}}{L_{\mathrm{Ln}}} & 0 & 0 & k_{\mathrm{vLin}}\\ \frac{k_{\mathrm{iLin}}v_{\mathrm{F0}}}{L_{\mathrm{Ln}}} & 0 & 0 & 0\end{bmatrix}^T \tag{A3}$$

$$\boldsymbol{B}_{\mathrm{Ln}}=\begin{bmatrix}\frac{g_0}{L_{\mathrm{Ln}}} & 0 & 0 & 0\end{bmatrix}^T \tag{A4}$$

$$\boldsymbol{C}_{\mathrm{bn}}=\begin{bmatrix}\frac{1-d_0+k_{\mathrm{pn}}i_{\mathrm{b0}}}{C_{sn}} & \frac{k_{\mathrm{pn}}C_{\mathrm{virbn}}i_{\mathrm{b0}}}{2TC_{sn}v_{\mathrm{bn}}} & -\frac{k_{in}i_{\mathrm{b0}}}{C_{sn}}\end{bmatrix} \tag{A5}$$

$$\boldsymbol{C}_{\mathrm{Ln}}=\begin{bmatrix}\frac{-g_0+k_{\mathrm{iLpn}}i_{\mathrm{L0}}}{C_{\mathrm{Fn}}}\\ \frac{k_{\mathrm{iLpn}}k_{\mathrm{vLpn}}i_{\mathrm{L0}}}{C_{\mathrm{Fn}}}\\ -\frac{k_{\mathrm{iLpn}}k_{\mathrm{vLin}}i_{\mathrm{L0}}}{C_{\mathrm{Fn}}}\\ -\frac{k_{\mathrm{iLin}}i_{\mathrm{L0}}}{C_{\mathrm{Fn}}}\end{bmatrix}^T \tag{A6}$$

$$D_{\mathrm{bn}}=\frac{2k_{\mathrm{pn}}K_{\mathrm{droopn}}v_{\mathrm{o0}}i_{\mathrm{b0}}}{C_{sn}v_{\mathrm{bn}}}+\frac{k_{\mathrm{pn}}C_{\mathrm{virbn}}v_{\mathrm{o0}}i_{\mathrm{b0}}}{TC_{sn}v_{\mathrm{bn}}}-\frac{k_{\mathrm{pn}}K_{\mathrm{droopn}}v_{\mathrm{oN}}i_{\mathrm{b0}}}{C_{sn}v_{\mathrm{bn}}} \tag{A7}$$

$$\boldsymbol{D}=\begin{bmatrix}D_{\mathrm{b1}} & 0 & 0 & 0 & 0 & 0 & 0\\ 0 & D_{\mathrm{b2}} & 0 & 0 & 0 & 0 & 0\\ 0 & 0 & D_{\mathrm{b3}} & 0 & 0 & 0 & 0\\ 0 & 0 & 0 & 0 & 0 & 0 & 0\\ 0 & 0 & 0 & 0 & 0 & 0 & 0\\ 0 & 0 & 0 & 0 & 0 & 0 & 0\\ 0 & 0 & 0 & 0 & 0 & 0 & 0\end{bmatrix} \tag{A8}$$

$$\boldsymbol{C}=\begin{bmatrix}-\frac{1}{C_{\mathrm{s1}}} & 0 & 0 & 0 & 0 & 0\\ 0 & -\frac{1}{C_{\mathrm{s2}}} & 0 & 0 & 0 & 0\\ 0 & 0 & -\frac{1}{C_{\mathrm{s3}}} & 0 & 0 & 0\\ \frac{1}{C_{\mathrm{DC}}} & \frac{1}{C_{\mathrm{DC}}} & \frac{1}{C_{\mathrm{DC}}} & -\frac{1}{C_{\mathrm{DC}}} & -\frac{1}{C_{\mathrm{DC}}} & -\frac{1}{C_{\mathrm{DC}}}\\ 0 & 0 & 0 & \frac{1}{C_{\mathrm{F1}}} & 0 & 0\\ 0 & 0 & 0 & 0 & \frac{1}{C_{\mathrm{F2}}} & 0\\ 0 & 0 & 0 & 0 & 0 & \frac{1}{C_{\mathrm{F3}}}\end{bmatrix} \tag{A9}$$

$$\boldsymbol{L}=\begin{bmatrix}\frac{1}{L_{\mathrm{s1}}} & 0 & 0 & -\frac{1}{L_{\mathrm{s1}}} & 0 & 0 & 0\\ 0 & \frac{1}{L_{\mathrm{s2}}} & 0 & -\frac{1}{L_{\mathrm{s2}}} & 0 & 0 & 0\\ 0 & 0 & \frac{1}{L_{\mathrm{s3}}} & -\frac{1}{L_{\mathrm{s3}}} & 0 & 0 & 0\\ 0 & 0 & 0 & \frac{1}{L_{\mathrm{F1}}} & -\frac{1}{L_{\mathrm{F1}}} & 0 & 0\\ 0 & 0 & 0 & \frac{1}{L_{\mathrm{F2}}} & 0 & -\frac{1}{L_{\mathrm{F2}}} & 0\\ 0 & 0 & 0 & \frac{1}{L_{\mathrm{F3}}} & 0 & 0 & -\frac{1}{L_{\mathrm{F3}}}\end{bmatrix} \tag{A10}$$

$$\boldsymbol{R}=\begin{bmatrix}-\frac{R_{\mathrm{s1}}}{L_{\mathrm{s1}}} & 0 & 0 & 0 & 0 & 0\\ 0 & -\frac{R_{\mathrm{s2}}}{L_{\mathrm{s2}}} & 0 & 0 & 0 & 0\\ 0 & 0 & -\frac{R_{\mathrm{s3}}}{L_{\mathrm{s3}}} & 0 & 0 & 0\\ 0 & 0 & 0 & -\frac{R_{\mathrm{F1}}}{L_{\mathrm{F1}}} & 0 & 0\\ 0 & 0 & 0 & 0 & -\frac{R_{\mathrm{F2}}}{L_{\mathrm{F2}}} & 0\\ 0 & 0 & 0 & 0 & 0 & -\frac{R_{\mathrm{F3}}}{L_{\mathrm{F3}}}\end{bmatrix} \tag{A11}$$

$$\boldsymbol{D}_{\mathrm{d123}}=\begin{bmatrix}\boldsymbol{D} & \boldsymbol{C}\\ \boldsymbol{L} & \boldsymbol{R}\end{bmatrix}. \tag{A12}$$

REFERENCES

[1] Z. Liu, M. Su, Y. Sun, W. Yuan, H. Han, and J. Feng, "Existence and stability of equilibrium of dc microgrid with constant power loads," *IEEE Trans. Power Syst.*, vol. 33, no. 6, pp. 6999–7010, Nov. 2018.

[2] S. Shao et al., "Modeling and advanced control of dual-active-bridge dc–dc converters: A review," *IEEE Trans. Power Electron.*, vol. 37, no. 2, pp. 1524–1547, Feb. 2022.

[3] L. Xu et al., "A review of dc shipboard microgrids—Part II: Control architectures, stability analysis, and protection schemes," *IEEE Trans. Power Electron.*, vol. 37, no. 4, pp. 4105–4120, Apr. 2022.

[4] W. Pei, X. Zhang, W. Deng, C. Tang, and L. Yao, "Review of operational control strategy for dc microgrids with electric-hydrogen hybrid storage systems," *CSEE J. Power Energy Syst.*, vol. 8, no. 2, pp. 329–346, 2022.

[5] H. Liu, W. Guo, D. Cheng, Y. Wang, and M. Wang, "Stability and bifurcation analysis of dc microgrid with multiple droop control sources and loads," *IEEE Trans. Power Electron.*, vol. 36, no. 2, pp. 2361–2372, Feb. 2021.

[6] Q. Xu, N. Vafamand, L. Chen, T. Dragičević, L. Xie, and F. Blaabjerg, "Review on advanced control technologies for bidirectional dc/dc converters in dc microgrids," *IEEE J. Emerg. Sel. Topics Power Electron.*, vol. 9, no. 2, pp. 1205–1221, Apr. 2021.

[7] M. Su, Z. Liu, Y. Sun, H. Han, and X. Hou, "Stability analysis and stabilization methods of dc microgrid with multiple parallel-connected dc–dc converters loaded by CPLs," *IEEE Trans. Smart Grid*, vol. 9, no. 1, pp. 132–142, Jan. 2018.

[8] F. Gao, R. Kang, J. Cao, and T. Yang, "Primary and secondary control in dc microgrids: A review," *J. Modern Power Syst. Clean Energy*, vol. 7, no. 2, pp. 227–242, 2019.

[9] W. W. A. G. Silva, T. R. Oliveira, and P. F. Donoso-Garcia, "An improved voltage-shifting strategy to attain concomitant accurate power sharing and voltage restoration in droop-controlled dc microgrids," *IEEE Trans. Power Electron.*, vol. 36, no. 2, pp. 2396–2406, Feb. 2021.

[10] X. Zhu, F. Meng, Z. Xie, and Y. Yue, "An inertia and damping control method of dc–dc converter in dc microgrids," *IEEE Trans. Energy Convers.*, vol. 35, no. 2, pp. 799–807, Jun. 2020.

[11] Y. Men, Y. Du, and X. Lu, "Distributed control framework and scalable small-signal stability analysis for dynamic microgrids," *Chin. J. Elect. Eng.*, vol. 7, no. 4, pp. 49–59, 2021.

[12] J. Sun, "Impedance-based stability criterion for grid-connected inverters," *IEEE Trans. Power Electron.*, vol. 26, no. 11, pp. 3075–3078, Nov. 2011.

[13] Y. Xu, H. Nian, B. Hu, and D. Sun, "Impedance modeling and stability analysis of VSG controlled type-IV wind turbine system," *IEEE Trans. Energy Convers.*, vol. 36, no. 4, pp. 3438–3448, Dec. 2021.

[14] J. Luo, S. Bu, and C. Y. Chung, "Design and comparison of auxiliary resonance controllers for mitigating modal resonance of power systems integrated with wind generation," *IEEE Trans. Power Syst.*, vol. 36, no. 4, pp. 3372–3383, Jul. 2021.

[15] W. Du, W. Dong, Y. Wang, and H. Wang, "Small-disturbance stability of a wind farm with virtual synchronous generators under the condition of weak grid connection," *IEEE Trans. Power Syst.*, vol. 36, no. 6, pp. 5500–5511, Nov. 2021.

[16] Y. Wang, C. Zhao, and R. Iravani, "Small signal stability investigation of the MMC-HVDC grid," *IEEE Trans. Power Del.*, vol. 37, no. 5, pp. 4448–4459, Oct. 2022.

[17] J. Luo, N. Tong, S. Bu, A. Meng, and H. Yin, "Internal modal resonance analysis for full converter-based wind generation using analytical inertia model," *IEEE Trans. Power Syst.*, early access, doi: 10.1109/TPWRS.2023.3287914.

[18] L. Fan and Z. Miao, "Admittance-based stability analysis: Bode plots, Nyquist diagrams or eigenvalue analysis?," *IEEE Trans. Power Syst.*, vol. 35, no. 4, pp. 3312–3315, Jul. 2020.

[19] X. Lu, W. Xiang, W. Lin, and J. Wen, "Comparative study of small-signal stability under weak AC system integration for different VSCs," *IEEE J. Emerg. Sel. Topics Power Electron.*, vol. 9, no. 4, pp. 4482–4499, Aug. 2021.

[20] H. Yang, T. Li, Y. Long, C. L. P. Chen, and Y. Xiao, "Distributed virtual inertia implementation of multiple electric springs based on model predictive control in dc microgrids," *IEEE Trans. Ind. Electron.*, vol. 69, no. 12, pp. 13 439–13 450, Dec. 2022.

[21] S. Anand and B. G. Fernandes, "Reduced-order model and stability analysis of low-voltage dc microgrid," *IEEE Trans. Ind. Electron.*, vol. 60, no. 11, pp. 5040–5049, Nov. 2013.

[22] A. Hosseinipour and H. Hojabri, "Small-signal stability analysis and active damping control of dc microgrids integrated with distributed electric springs," *IEEE Trans. Smart Grid*, vol. 11, no. 5, pp. 3737–3747, Sep. 2020.

[23] H. Kirchhoff and K. Strunz, "Control and stability of modular dc swarm microgrids," *IEEE J. Emerg. Sel. Topics Power Electron.*, vol. 10, no. 5, pp. 6274–6292, Oct. 2022.

[24] B. Wang and G. Verbič, "Stability analysis of low-voltage distribution feeders operated as islanded microgrids," *IEEE Trans. Smart Grid*, vol. 12, no. 6, pp. 4681–4689, Nov. 2021.

[25] W. Du, K. Zheng, and H. Wang, "Oscillation instability of a dc microgrid caused by aggregation of same constant power loads in parallel connection," *IET Gener. Transmiss. Distrib.*, vol. 13, no. 13, pp. 2637–2645, 2019.

[26] W. Du, W. Dong, and H. Wang, "A method of reduced-order modal computation for planning grid connection of a large-scale wind farm," *IEEE Trans. Sustain. Energy*, vol. 11, no. 3, pp. 1185–1198, Jul. 2020.

[27] M. F. M. Arani and Y. A. -R. I. Mohamed, "Analysis and performance enhancement of vector-controlled VSC in HVDC links connected to very weak grids," *IEEE Trans. Power Syst.*, vol. 32, no. 1, pp. 684–693, Jan. 2017.

[28] B. Zhang, F. Gao, Y. Zhang, D. Liu, and H. Tang, "An ac-dc coupled droop control strategy for VSC-based dc microgrids," *IEEE Trans. Power Electron.*, vol. 37, no. 6, pp. 6568–6584, Jun. 2022.

[29] G. Lin et al., "A virtual inertia and damping control to suppress voltage oscillation in islanded dc microgrid," *IEEE Trans. Energy Convers.*, vol. 36, no. 3, pp. 1711–1721, Sep. 2021.

[30] M. N. Hussain, G. Melath, and V. Agarwal, "An active damping technique for PI and predictive controllers of an interlinking converter in an islanded hybrid microgrid," *IEEE Trans. Power Electron.*, vol. 36, no. 5, pp. 5521–5529, May 2021.

[31] P. Strajnikov, M. M. Peretz, and A. Kuperman, "Reduced-rating-electronic-capacitor-based dc links for power electronics supported distributed energy resources," *IEEE Trans. Smart Grid*, vol. 13, no. 5, pp. 3943–3953, Sep. 2022.

[32] A. Maulik and D. Das, "Stability constrained economic operation of islanded droop-controlled dc microgrids," *IEEE Trans. Sustain. Energy*, vol. 10, no. 2, pp. 569–578, Apr. 2019.

[33] Y. Reddy, O. J. Jithendranath, A. K. Chakraborty, and J. M. Guerrero, "Stability constrained optimal operation of standalone dc microgrids considering load and solar PV uncertainties," *IEEE Trans. Power Del.*, vol. 38, no. 4, pp. 2673–2681, Aug. 2023.

[34] M. N. Hussain and V. Agarwal, "Optimal placement of constant power loads at different buses of a dc microgrid ensuring maximum stability margins," *IEEE J. Emerg. Sel. Topics Power Electron.*, vol. 9, no. 1, pp. 510–519, Feb. 2021.

Ling Yang (Member, IEEE) was born in Liaoning, China, in 1992. She received the B.S. and Ph.D. degrees in electrical engineering from Hunan University, Changsha, China, in 2014 and 2019, respectively.

She is currently an Associate Professor with the School of Automation, Guangdong University of Technology, Guangzhou, China. Her research interests include power electronics and distributed power systems.

Zehang Huang (Student Member, IEEE) was born in Guangdong, China, in 1997. He received the B.S. degree in electrical engineering from Huizhou University, Huizhou, China, in 2020. He is currently working toward the M.S. degree with the Guangdong University of Technology, Guangzhou, China.

His research interests include renewable energy generation technology.

Jinghua Chen was born in Jiangxi, China, in 1974. She received the B.S. degree in electrical engineering from Nanchang University, Nanchang, China, in 1997, and the M.S. and Ph.D. degrees in control engineering from the Guangdong University of Technology, Guangzhou, China, in 2001 and 2007, respectively.

She is currently an Associate Professor with the School of Automation, Guangdong University of Technology. Her research interests include power system operation optimization and control.

Jianqiang Luo (Member, IEEE) received the B.Eng. and M.Eng. degrees in electrical engineering from the Huazhong University of Science and Technology, Wuhan, China, in 2010 and 2015, respectively, and the Ph.D. degree in electrical engineering from Hong Kong Polytechnic University, Hong Kong, in 2021.

He was a visiting doctoral student with Imperial College London, London, U.K., in 2020. He is currently an Associate Professor with the Guangdong University of Technology, Guangzhou, China, and also a National Registered Electrical Engineer. His research interests include power system stability analysis and the application of artificial intelligence in power systems.

Yu Wang (Member, IEEE) was born in Guangdong, China, in 1984. He received the B.S. degree in electronic engineering from Nanchang Hangkong University, Nanchang, China, in 2007, the M.S. degree in control engineering from Guangxi University, Nanning, China, in 2010, and the Ph.D. degree in power electronics from the South China University of Technology, Guangzhou, China, in 2015.

From 2015 to 2017, he was a Postdoctoral Researcher with the Department of Electrical Engineering, Tsinghua University, Beijing, China. Since 2018, he has been an Associate Professor with the School of Automation, Guangdong University of Technology, Guangzhou. From 2019 to 2020, he was an ERCIM "Alain Bensoussan" Research Fellow with the Department of Electric Power Engineering, Norwegian University of Science and Technology, Trondheim, Norway. His current research interests include high-frequency power electronic solid-state transformer and the flexible dc transmission and distribution systems.

Marta Molinas (Fellow, IEEE) received the Diploma degree in electromechanical engineering from the National University of Asuncion, Asuncion, Paraguay, in 1992, the Master of Engineering degree in electrical engineering from Ryukyu University, Nishihara, Japan, in 1997, and the Doctor of Engineering degree in electrical engineering from the Tokyo Institute of Technology, Tokyo, Japan, in 2000.

She was a Guest Researcher with the University of Padova, Padova, Italy, in 1998. She is currently a Professor with the Department of Engineering Cybernetics, Norwegian University of Science and Technology, Trondheim, Norway, where she was a Postdoctoral Researcher from 2004 to 2007 and a Professor with the Department of Electric Power Engineering from 2008 to 2014. Her research interests include stability of power electronics systems, harmonics, instantaneous frequency, and nonstationary signals from the human and the machine.

Dr. Molinas is an Editor for IEEE JOURNAL OF EMERGING AND SELECTED TOPICS IN POWER ELECTRONICS, an Associate Editor for IEEE TRANSACTIONS ON POWER ELECTRONICS, and an Editor for IEEE TRANSACTIONS ON ENERGY CONVERSION. She was an AdCom Member of the IEEE Power Electronics Society from 2009 to 2011.

Olav Bjarte Fosso (Senior Member, IEEE) received the Ph.D. degree in electrical engineering from the Norwegian Institute of Technology, Trondheim, Norway, in 1989.

He is currently a Professor with the Department of Electric Power Engineering, Norwegian University of Science and Technology (NTNU), Trondheim. He was a Scientific Advisor and a Senior Research Scientist with SINTEF Energy Research, Trondheim, and the Director of NTNU's Strategic Thematic Area Energy from 2014 to 2016. He was an expert evaluator in Horizon2020 and several science foundations, internationally. His research interests include hydro scheduling, market integration of intermittent generation, and signal analysis for study of power system's dynamics and stability.

Dr. Fosso was the Chairman of the CIGRE Study Committee C5 "Electricity Markets and Regulation" and a Member of the CIGRE Technical Committee from 2008 to 2014.